

Possible topological phases in quantum anomalous Hall insulator/unconventional superconductor hybrid systems

Ryoi Ohashi¹, Shingo Kobayashi², and Yukio Tanaka¹

¹Department of Applied Physics, Nagoya University, Nagoya 464-8603, Japan

²RIKEN Center for Emergent Matter Science, Wako, Saitama 351-0198, Japan

(Received 22 July 2021; revised 18 October 2021; accepted 19 October 2021; published 28 October 2021)

Quantum anomalous Hall insulator (QAH)/*s*-wave superconductor (SC) hybrid systems are known to be an ideal platform for realizing two-dimensional topological superconductors with chiral Majorana edge modes. In this paper we study QAH/unconventional SC hybrid systems whose pairing symmetry is *p* wave, *d* wave, chiral *p* wave, or chiral *d* wave. The hybrid systems are a generalization of the QAH/*s*-wave SC hybrid system. In view of the symmetries of the QAH and pairings, we introduce three topological numbers to classify the topological phases of the hybrid systems. One is the Chern number, which characterizes chiral Majorana edge modes, and the others are topological numbers associated with crystalline symmetries. We numerically calculate the topological numbers and associated surface states for three characteristic regimes that feature the influence of unconventional SCs on QAHs. Our calculation shows a rich variety of topological phases and unveils the following topological phases that are not counterparts of the *s*-wave case: crystalline symmetry-protected helical Majorana edge modes, a line node phase (a crystalline-symmetry-protected Bogoliubov Fermi surface), and multiple chiral Majorana edge modes. The phenomena result from a nontrivial topological interplay between the QAH and unconventional SCs. Finally, we discuss tunnel conductance in a junction between a normal metal and the hybrid systems and show that the chiral and helical Majorana edge modes are distinguishable in terms of the presence or absence of a zero-bias conductance peak.

DOI: [10.1103/PhysRevB.104.134518](https://doi.org/10.1103/PhysRevB.104.134518)

I. INTRODUCTION

Unconventional superconductors (SCs) with nonzero topology, dubbed topological SCs, have been the subject of intense study [1–8] since they host Majorana fermions on their surface as surface zero-energy Andreev bound states. The Majorana fermions follow non-Abelian statistics [9–14] and have been proposed as a topological qubit to implement fault-tolerant topological quantum computation [15]. To realize emergent Majorana fermions, a lot of efforts have been devoted to one-dimensional systems, such as semiconductor/SC hybrid systems [16–27] and a magnetic atomic chain on superconductors [28–37].

Alongside those efforts, quantum anomalous Hall insulator (QAH)/SC hybrid systems have attracted a lot of interest as another platform for topological SCs. QAHs are two-dimensional (2D) topological insulators that exhibit quantized Hall conductance without an external magnetic field and host chiral fermions on the edge [38–40]. The QAHs in proximity to an *s*-wave SC become 2D topological SCs [41–44]. Due to the breaking of time-reversal symmetry (TRS), the superconducting states belong to class D of the Altland-Zirnbauer symmetry classes [45–50]. The topological phases are characterized by the Chern number \mathcal{N} . Figure 1 shows the phase diagram of QAH/*s*-wave SC hybrid systems, where m is a mass parameter and Δ_0 is the amplitude of the gap function. The phases with $\mathcal{N} = 2$, 1, and 0 indicate the presence of two, one, and zero chiral Majorana edge modes, respectively. Recent experiments on QAH/topological SC/QAH junctions

observed a half-quantized conductance [51], which signals the $\mathcal{N} = 1$ phase [52–54], i.e., a single Majorana chiral edge mode, but its existence is still open to debate [55–59].

Recently, QAH/SC hybrid systems have been generalized to hybrid systems with antiferromagnetic topological insulators [57,60], *s*-wave SC with nontrivial topology [61], or *d*-wave SCs [62]. Interestingly, such extended hybrid systems bring other 2D topological phases showing helical Majorana edge modes protected by a pseudo-TRS [57] and multiple chiral Majorana edge modes [60–62]. These exotic

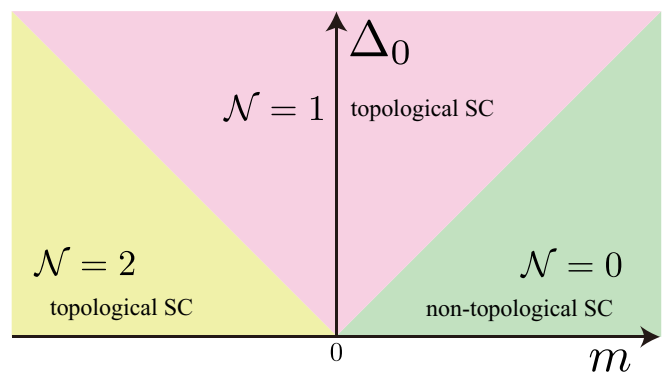


FIG. 1. Phase diagram of the QAH/*s*-wave SC hybrid system [41,44]. Here, m and Δ_0 represent the mass gap and the amplitude of the *s*-wave pair potential, respectively. \mathcal{N} indicates the Chern number for each phase.

topological surface states have provided another route for probing Majorana edge modes [61,62]. In addition, superconducting doped topological materials, including topological insulators [63–66] and Dirac/Weyl semimetals [67–72], are a promising platform to explore topological superconductivity induced by topologically nontrivial electron states.

In this paper, we study topological phases of QAH/unconventional SC hybrid systems as a generalization of the QAH/*s*-wave SC hybrid system. Unconventional SCs, which have non-*s*-wave pairing, can be realized in cuprates [73–75], Sr₂RuO₄ [76–86], SrPtAs [87–89], heavy-fermion materials [90–98], and so on. We consider *p*-wave, *d*-wave, chiral *p*-wave, and chiral *d*-wave pairings as possible non-*s*-wave pairings on the SC side and examine a superconducting state realized by the topological interplay between these pairings and the QAH.

Numerically calculating surface states and topological numbers peculiar to QAH/unconventional SC hybrid systems, we show that the hybrid systems exhibit versatile topological phases with no counterpart of the QAH/*s*-wave SC hybrid system; these topological phases are attributed to nontrivial topology or spin structures in unconventional Cooper pairs. For instance, chiral SCs manifest a nontrivial Chern number ($\mathcal{N} \neq 0$). Thus, a nontrivial topological interplay may emerge in the hybrid systems. We discuss possible topological phases for three characteristic parameter regimes: (i) $E_g > 2|\Delta_0|$, (ii) $E_g < 2|\Delta_0|$, and (iii) the metallic state, where E_g is the amplitude of the insulating gap in the QAH and the metallic state is the situation where the chemical potential lies above or below the insulating gap. The topological properties of hybrid systems for each parameter regime are briefly summarized as follows. Hereafter, we assume topologically nontrivial states in the underlying QAHs.

(i) Only a chiral edge mode is contributed to the superconducting state for $E_g > 2|\Delta_0|$, thereby leading to two chiral Majorana edge modes irrespective of pairing symmetries.

(ii) Different topological phases appear for some pairing symmetries when the gap function satisfies $E_g < 2|\Delta_0|$. We find a crystalline-symmetry-protected helical Majorana edge mode when the pairing symmetry is a *p*-wave pairing. Moreover, a gapless phase appears when an inconsistency occurs between the spin structures of the QAH and spin-triplet pairing. The gapless phase is regarded as a crystalline-symmetry-protected Bogoliubov Fermi surface.

(iii) Topological phases inherent in unconventional pairings appear when the chemical potential lies at the bulk bands; if the pair potential has nodes, zero-energy flat bands or sine-curved states are realized on the surface. On the other hand, if it has a full gap, we find multiple chiral Majorana edge modes, the number of which is determined from a sum rule of the Chern number. In addition, the gapless phase mentioned above appears again since it is attributed to the mismatch of the spin structures.

Finally, we discuss tunnel conductance in a normal metal/(QAH/SC) junction as a probe to distinguish the crystalline-symmetry-protected helical Majorana edge modes from the chiral ones; the former exhibits a sharp zero-bias conductance peak mediated by the zero-energy states protected by crystalline symmetry, whereas the latter does not due to the interference of the zero-energy states [99].

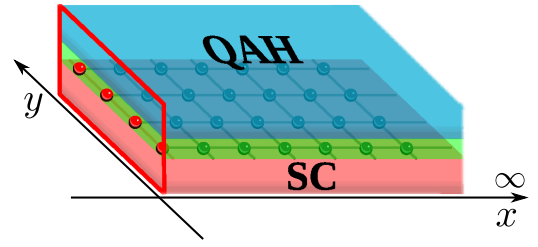


FIG. 2. Schematic illustration of QAH/SC hybrid systems.

This paper is organized as follows. We formulate QAH/unconventional SC hybrid systems in Sec. II A. The symmetries and topological numbers are summarized in Secs. II B and II C. The numerical method is introduced in Sec. II D. In Sec. III A, we give an overview of our findings for three characteristic parameter regimes in the QAH/unconventional SC hybrid systems. In particular, we discuss topological properties and surface states for crystalline-symmetry-protected helical Majorana edge modes, a crystalline-symmetry-protected Bogoliubov Fermi surface, and multiple chiral Majorana edge modes in Secs. III B, III C, and III D, respectively. The relations to the tunnel conductance are discussed in Sec. IV, and a summary is given.

II. QAH/SC MODEL

A. Formulation

We start from a minimum two-dimensional Hamiltonian describing QAH states, $\mathcal{H}_{\text{QAH}} = \sum_{\mathbf{k}} \psi_{\mathbf{k}}^{\dagger} H_{\text{QAH}}(\mathbf{k}) \psi_{\mathbf{k}}$, with $\psi_{\mathbf{k}} = (c_{k,\uparrow}, c_{k,\downarrow})^T$ and

$$H_{\text{QAH}}(\mathbf{k}) = m(\mathbf{k})\sigma_z + A(k_x\sigma_x + k_y\sigma_y), \quad (1)$$

where $m(\mathbf{k}) = m + B(k_x^2 + k_y^2)$, A , and σ_i are a mass term, a spin-orbital coupling term, and the Pauli matrices in the spin space, respectively. The mass term breaks TRS and opens a gap at $\mathbf{k} = 0$; the energy spectrum is given by $E_{\text{QAH}}(\mathbf{k}) \equiv \sqrt{A^2(k_x^2 + k_y^2) + [m + B(k_x^2 + k_y^2)]^2}$, leading to the insulating gap $E_g = 2|m|$. For $m/B < 0$, the system belongs to the QAH phase with a single chiral edge mode on the boundary [41].

Using Eq. (1), we model the QAH/SC hybrid system, where the QAH is supposed to be stacked on an SC (see Fig. 2). In the hybrid system, Cooper pairs in the SC are induced to the QAH due to the proximity effect, and thus, the QAH/SC system can be described by the Bogoliubov-de Gennes (BdG) Hamiltonian, $\mathcal{H}_{\text{BdG}} = \frac{1}{2} \sum_{\mathbf{k}} \Psi_{\mathbf{k}}^{\dagger} H_{\text{BdG}}(\mathbf{k}) \Psi_{\mathbf{k}}$, with $\Psi_{\mathbf{k}} = (c_{k,\uparrow}, c_{k,\downarrow}, c_{-k,\uparrow}^{\dagger}, c_{-k,\downarrow}^{\dagger})^T$ and

$$H_{\text{BdG}}(\mathbf{k}) = \begin{pmatrix} H_{\text{QAH}}(\mathbf{k}) - \mu & \Delta(\mathbf{k}) \\ \Delta^{\dagger}(\mathbf{k}) & -H_{\text{QAH}}^*(-\mathbf{k}) + \mu \end{pmatrix}, \quad (2)$$

where μ is the chemical potential and $\Delta(\mathbf{k})$ is the induced gap function. In the following, we consider unconventional SCs, and thus, $\Delta(\mathbf{k})$ describes non-*s*-wave Cooper pairings such as *p*-wave, *d*-wave, chiral *p*-wave, and chiral *d*-wave pairs. For spin-singlet Cooper pairings, we define the gap function as

$$\Delta(\mathbf{k}) = \Delta_0 f(\mathbf{k})(i\sigma_y), \quad (3)$$

where the form factor $f(\mathbf{k})$ depends on Cooper pair symmetry such that

$$f(\mathbf{k}) = \begin{cases} 1 & (s \text{ wave}), \\ k_x k_y & (d_{xy} \text{ wave}), \\ k_x^2 - k_y^2 & (d_{x^2-y^2} \text{ wave}), \\ (k_x \pm ik_y)^2 & (\text{chiral } d \pm id \text{ wave}). \end{cases} \quad (4)$$

We note that the d_{xy} -wave ($d_{x^2-y^2}$ -wave) pairing hosts point nodes at $k_x = 0$ and $k_y = 0$ ($k_x = k_y$ and $k_x = -k_y$) on the Fermi surface, whereas the chiral ($d \pm id$)-wave pairing has a full gap and breaks TRS spontaneously.

On the other hand, the gap function in spin-triplet Cooper pairings is formally described as

$$\Delta(\mathbf{k}) = \Delta_0 \mathbf{d}(\mathbf{k}) \cdot \boldsymbol{\sigma}(i\sigma_y), \quad (5)$$

with $\mathbf{d}(\mathbf{k}) = (d_x(\mathbf{k}), d_y(\mathbf{k}), d_z(\mathbf{k}))$. The \mathbf{d} vector represents the spin degrees of freedom of Cooper pairs. The p_v -wave and chiral p -wave pairings are represented by the \mathbf{d} vector with

$$d_i(\mathbf{k}) = \begin{cases} k_\nu & (p_\nu \text{ wave}), \\ k_x \pm ik_y & (\text{chiral } p \pm ip \text{ wave}) \end{cases} \quad (6)$$

and $d_j = 0$ when $j \neq i$, where $\nu = x, y$ and $i = x, y, z$. For the chiral ($p \pm ip$)-wave pair, we fix the \mathbf{d} vector along the z direction. Note that the p_x - and p_y -wave pairings have a pair of point nodes at $k_x = 0$ and $k_y = 0$ on the Fermi surface, respectively.

B. Symmetries

In the following, we summarize the symmetries of the QAH/SC hybrid systems, which are useful to define the topological numbers in Sec II C. First, let us consider the symmetries of the normal Hamiltonian (1). In the QAH, TRS ($T = i\sigma_y \mathcal{K}$) is absent, but crystalline symmetries that keep the Hamiltonian (1) invariant exist. Equation (1) satisfies twofold rotation symmetry in the z axis,

$$C_{2z} H_{\text{QAH}}(\mathbf{k}) C_{2z}^{-1} = H_{\text{QAH}}(-\mathbf{k}), \quad C_{2z} = i\sigma_z. \quad (7)$$

In addition, although twofold rotation symmetries in terms of the x and y axis (C_{2x} and C_{2y}) are not symmetries of the Hamiltonian, the combination with TRS keeps the Hamiltonian invariant. That is, the combined operations, defined by $A_x = C_{2x} T$ and $A_y = C_{2y} T$, satisfy

$$A_x H_{\text{QAH}}(k_x, k_y) A_x^{-1} = H_{\text{QAH}}(-k_x, k_y), \quad A_x = \sigma_z \mathcal{K}, \quad (8)$$

$$A_y H_{\text{QAH}}(k_x, k_y) A_y^{-1} = H_{\text{QAH}}(k_x, -k_y), \quad A_y = \mathcal{K}, \quad (9)$$

which we call magnetic-reflection symmetry in this paper. Here, \mathcal{K} is the complex-conjugation operator.

Next, we consider symmetries of the QAH/SC hybrid systems (2) that break TRS but preserve particle-hole symmetry:

$$\mathcal{C} H_{\text{BdG}}(\mathbf{k}) \mathcal{C}^{-1} = -H_{\text{BdG}}(-\mathbf{k}), \quad \mathcal{C} = \tau_x \mathcal{K}, \quad (10)$$

where τ_i are the Pauli matrices in the Nambu space. Hence, our systems belong to class D of the Altland-Zirnbauer symmetry classes.

In addition, the crystalline symmetries (7), (8), and (9) are again symmetries of the BdG Hamiltonian, whose representations are modified due to pairing symmetry. The gap functions transform, under the action of $g = C_{2z}, A_x$, and A_y , as

$$g \Delta(\mathbf{k}) g^T = \pm \Delta(D_g \mathbf{k}), \quad (11)$$

TABLE I. Representations of crystalline symmetries in QAH/SC hybrid systems.

Pairing symmetry	C_{2z}	A_x	A_y	Γ_{A_x}	Γ_{A_y}
s wave	$i\sigma_z \tau_z$	$\sigma_z \tau_z \mathcal{K}$	\mathcal{K}	$\sigma_z \tau_y$	τ_x
d_{xy} wave	$i\sigma_z \tau_z$	$\sigma_z \mathcal{K}$	$\tau_z \mathcal{K}$	$\sigma_z \tau_x$	τ_y
$d_{x^2-y^2}$ wave	$i\sigma_z \tau_z$	$\sigma_z \tau_z \mathcal{K}$	\mathcal{K}	$\sigma_z \tau_y$	τ_x
Chiral $d \pm id$ wave	$i\sigma_z \tau_z$	$\sigma_z \tau_z \mathcal{K}$	\mathcal{K}	$\sigma_z \tau_y$	τ_x
p_x wave ($\mathbf{d} \parallel \hat{x}$)	$i\sigma_z \tau_z$	$\sigma_z \tau_z \mathcal{K}$	\mathcal{K}	$\sigma_z \tau_y$	τ_x
p_x wave ($\mathbf{d} \parallel \hat{y}$)	$i\sigma_z \tau_z$	$\sigma_z \mathcal{K}$	$\tau_z \mathcal{K}$	$\sigma_z \tau_x$	τ_y
p_x wave ($\mathbf{d} \parallel \hat{z}$)	$i\sigma_z$	$\sigma_z \mathcal{K}$	\mathcal{K}	$\sigma_z \tau_x$	τ_x
p_y wave ($\mathbf{d} \parallel \hat{x}$)	$i\sigma_z \tau_z$	$\sigma_z \mathcal{K}$	$\tau_z \mathcal{K}$	$\sigma_z \tau_x$	τ_y
p_y wave ($\mathbf{d} \parallel \hat{y}$)	$i\sigma_z \tau_z$	$\sigma_z \tau_z \mathcal{K}$	\mathcal{K}	$\sigma_z \tau_y$	τ_x
p_y wave ($\mathbf{d} \parallel \hat{z}$)	$i\sigma_z$	$\sigma_z \tau_z \mathcal{K}$	$\tau_z \mathcal{K}$	$\sigma_z \tau_y$	τ_y
Chiral $p \pm ip$ wave	$i\sigma_z$	$\sigma_z \mathcal{K}$	\mathcal{K}	$\sigma_z \tau_x$	τ_x

where D_g obeys the change in momentum in Eqs. (7), (8), and (9) and the plus and minus signs represent the parity of the gap functions in terms of g . Thus, to be consistent with Eq. (11), representations of g in the Nambu space are given by

$$\mathcal{G} = \begin{pmatrix} g & 0 \\ 0 & \pm g^* \end{pmatrix}, \quad (12)$$

where $+$ ($-$) comes from the parity of gap functions in Eq. (11). In the matrix representation, the BdG Hamiltonian and the particle-hole operator satisfy

$$\mathcal{G} H_{\text{BdG}}(\mathbf{k}) \mathcal{G}^{-1} = H_{\text{BdG}}(D_g \mathbf{k}), \quad \mathcal{C} \mathcal{G} = \pm \mathcal{G} \mathcal{C}, \quad (13)$$

where the sign reflects the parity of the gap function in Eq. (11). The explicit representations of $\mathcal{G} = C_{2z}, A_x$, and A_y are summarized in Table I. Here, we use calligraphic fonts for the symmetries in the BdG Hamiltonian.

Furthermore, the combination of \mathcal{G} and \mathcal{C} constitutes chiral operators, $\Gamma_{A_x} \equiv e^{i\phi} A_x \mathcal{C}$ and $\Gamma_{A_y} \equiv e^{i\phi'} A_y \mathcal{C}$, which satisfy

$$\Gamma_{A_x} H_{\text{BdG}}(k_x, k_y) \Gamma_{A_x}^{-1} = -H_{\text{BdG}}(k_x, -k_y), \quad (14)$$

$$\Gamma_{A_y} H_{\text{BdG}}(k_x, k_y) \Gamma_{A_y}^{-1} = -H_{\text{BdG}}(-k_x, k_y), \quad (15)$$

where we choose the phase factors ϕ and ϕ' as $\Gamma_{A_x}^2 = \Gamma_{A_y}^2 = \mathbf{1}_{4 \times 4}$, with $\mathbf{1}_{N \times N}$ being the $N \times N$ identity matrix. These chiral operators are defined for all gap functions; see the rightmost columns in Table I.

C. Topological numbers

We here discuss possible topological numbers inherent in the symmetries of the QAH/SC hybrid system.

1. Chern number

Since the QAH/SC hybrid systems break TRS, we can define the Chern number \mathcal{N} as

$$\mathcal{N} = \sum_{n \in \text{occ}} \int_{\text{BZ}} \frac{d^2 \mathbf{k}}{2\pi} \left(\frac{\partial a_{n,y}}{\partial k_x} - \frac{\partial a_{n,x}}{\partial k_y} \right), \quad (16)$$

$$a_{n,i} = -i \langle u_{n,\mathbf{k}} | \frac{\partial}{\partial k_i} | u_{n,\mathbf{k}} \rangle, \quad (17)$$

when the energy spectrum is fully gapped over the 2D Brillouin zone (BZ). Here, $|u_{n,\mathbf{k}}\rangle$ is an eigenstate of $H_{\text{BdG}}(\mathbf{k})$

with a band label n and momentum \mathbf{k} , and the summation is taken over the occupied states. The Chern number corresponds to the number of chiral Majorana edge modes through the bulk-boundary correspondence, and its sign is related to the direction of edge currents; for instance, chiral Majorana edge modes associated with the Chern numbers $\mathcal{N} = 1$ and -1 propagate in opposite directions. In the QAH/ s -wave SC hybrid systems, the Chern number takes $\mathcal{N} = 0, 1$, and 2 (see Fig. 1).

2. One-dimensional winding number classified by \mathbb{Z}

The QAH/SC systems host additional crystalline symmetries (13), (14), and (15) which allow us to define crystalline-symmetry-protected topological numbers. Using the chiral symmetries [Eqs. (14) and (15)], we can define a crystalline-symmetry-protected one-dimensional (1D) winding number [43,100] in a 1D subspace of the BZ,

$$\mathcal{W}[\Gamma_{\mathcal{A}_i}] = \frac{i}{4\pi} \int_{-\pi}^{\pi} dk_i \text{Tr} \left[\Gamma_{\mathcal{A}_i} H_{\text{BdG}}^{-1}(\mathbf{k}) \frac{\partial}{\partial k_i} H_{\text{BdG}}(\mathbf{k}) \right], \quad (18)$$

where we fix $k_x = 0$ for $\Gamma_{\mathcal{A}_y}$ and $k_y = 0$ for $\Gamma_{\mathcal{A}_x}$. The nonzero 1D winding number ensures the existence of zero-energy modes at the edges of the 1D subspace through the bulk-boundary correspondence. The 1D winding number is intrinsically related to the Chern number, so $|\mathcal{W}[\Gamma_{\mathcal{A}_i}]|$ counts the number of chiral Majorana edge modes that cut across $k_x = 0$ or $k_y = 0$ in the surface BZ. For instance, when we consider the QAH/ s -wave SC hybrid system and impose the open (periodic) boundary condition in the x (y) direction, $\mathcal{W}[\Gamma_{\mathcal{A}_x}]$ describes zero modes at $k_y = 0$ in the surface BZ; the 1D winding number takes $\mathcal{W}[\Gamma_{\mathcal{A}_x}] = 1$ when $\mathcal{N} = 1$, while $\mathcal{W}[\Gamma_{\mathcal{A}_x}] = 0$ when $\mathcal{N} = 0, 2$ [43] because only a single chiral Majorana edge mode cuts across $k_y = 0$. Hereafter, we abbreviate $\mathcal{W}[\Gamma_{\mathcal{A}_i}]$ as \mathcal{W} unless otherwise specified.

3. Zero-dimensional topological number classified by \mathbb{Z}_2

In addition, the QAH/SC hybrid systems satisfy twofold rotation symmetry,

$$C_{2z} H_{\text{BdG}}(\mathbf{k}) C_{2z}^{-1} = H_{\text{BdG}}(-\mathbf{k}), \quad (19)$$

which leads to a crystalline symmetry-protected zero-dimensional (0D) \mathbb{Z}_2 invariant when the parity of the gap function is odd under C_{2z} , i.e., $\{C_{2z}, \mathcal{C}\} = 0$. Combining Eq. (19) with $\mathcal{C} = \tau_x \mathcal{K}$ in Eq. (10), the BdG Hamiltonian satisfies

$$(-i\tau_x C_{2z}) H_{\text{BdG}}(\mathbf{k}) = -[(-i\tau_x C_{2z}) H_{\text{BdG}}(\mathbf{k})]^T, \quad (20)$$

where we add $-i$ to make the operator real. Equation (20) indicates that the matrix is screw symmetric, and thus, we can define a Pfaffian invariant,

$$(-1)^\nu = \text{sgn} \left\{ \frac{\text{Pf}[(-i\tau_x C_{2z}) H_{\text{BdG}}(\mathbf{k}')] }{\text{Pf}[(-i\tau_x C_{2z}) H_{\text{BdG}}(\mathbf{k}'')] } \right\}, \quad (21)$$

which takes $\nu = 0, 1 \in \mathbb{Z}_2$ since $\text{Pf}[(-i\tau_x C_{2z}) H_{\text{BdG}}(\mathbf{k})] \in \mathbb{R}$. Here, \mathbf{k}' and \mathbf{k}'' are arbitrary wave numbers in the 2D BZ. If $\nu = 1 \pmod{2}$, a gapless point exists on a line connecting \mathbf{k}' and \mathbf{k}'' ; namely, one of the wave numbers is enclosed by a line node. In terms of topology, the line node is analogous to

the Bogoliubov Fermi surface [101–106]. Thus, we call it a crystalline-symmetry-protected Bogoliubov Fermi surface.

D. Numerical method

We numerically calculate the surface density of states (SDOS) and the topological numbers to explore topological surface states through the bulk-boundary correspondence. We perform the numerical calculation on a square lattice by replacing $k_i \rightarrow \sin k_i$ and $k_i^2 \rightarrow 2(1 - \cos k_i)$ in Eq. (2).

For SDOs, we impose the periodic boundary condition for the y axis and the semi-infinite boundary condition for the x axis (see Fig. 2). Using the surface Green's function $G_s(k_y, E)$, the angle-resolved SDOS is defined by

$$\rho(k_y, E) = -\frac{1}{\pi} \text{Im}[P_e G^R(k_y, E)], \quad (22)$$

with the retarded Green's function

$$G^R(k_y, E) = G_s(k_y, E + i\eta), \quad (23)$$

where E is the energy of the semi-infinite system, η is an infinitesimal positive number, and $P_e = (\tau_0 + \tau_z)/2$ is the projection onto the electron states. The surface Green's function in the semi-infinite system is obtained using Umerski's method [107].

For topological numbers, the Chern number (16) is calculated using the gauge-invariant method [108], where the Chern number is defined on the discretized Brillouin zone with a mesh size of $N_x \times N_y$, which approaches the exact Chern number when the mesh is sufficiently large. We choose $N_x = N_y = 512$ in this paper. The obtained Chern number is consistent with the results for SDOs. Similarly, the winding number (18) is calculated on the discretized Brillouin zone, where we directly replace the integral by a summation since Eq. (18) does not depend on the choice of the gauge. In the numerical calculation, we fix $k_y = 0$ and take a replacement $\int dk_x \rightarrow \frac{2\pi}{N_x} \sum$, with $N_x = 10\,000$.

In the following, we fix $A = 0.1$ and $B = 1$ and choose the other parameters to be $(m, \Delta_0, \mu) = (\pm 0.05, 0.025, 0)$, $(\pm 0.05, 0.025, 0.01)$, $(\pm 0.05, 0.175, 0)$, $(\pm 0.05, 0.175, 0.01)$, and $(\pm 0.05, 0.025, 0.06)$. The first and second parameters belong to the regime $E_g > 2|\Delta_0|$, the third and fourth belong to $E_g < 2|\Delta_0|$, and the fifth belongs to the metallic states, where $E_g = 2|m|$ is the insulating gap and $m < 0$ ($m > 0$) describes the topologically nontrivial (trivial) phases of the QAH. For $E_g > 2|\Delta_0|$ and $E_g < 2|\Delta_0|$, we also check the dependence of the chemical potential because an accidental degeneracy of surface zero-energy states occurs when $\mu = 0$, while it disappears when $\mu \neq 0$ [99].

III. RESULT

A. Overview

We apply the numerical methods to the QAH/unconventional SC hybrid systems. The results are summarized in Table II, where gap structures, surface states, and topological numbers are shown in the three parameter regimes. The SDOs on the (10) surface in the QAH/ s -wave, QAH/ p_x -wave, QAH/ p_y -wave, QAH/ d_{xy} -wave, QAH/ $d_{x^2-y^2}$ -wave SC hybrid systems are schematically

TABLE II. Summary of surface states (SSs) and bulk gap structures (GSs) in the QAH/unconventional SC hybrid systems, where we assume that the QAH is topologically nontrivial ($m < 0$) and the semi-infinite (periodic) boundary condition is imposed in the x (y) direction. Here, \mathcal{N} and \mathcal{W} represent the Chern number (16) and the winding number (18) defined at $k_y = 0$. The GSs are classified as a full gap, a point node, and a line node in the 2D BZ, where the line node is a crystalline-symmetry-protected Bogoliubov Fermi surface, as discussed in Sec. III C. For SSs, chiral Majorana edge modes (chiral) are stabilized by the Chern number, whereas the helical Majorana edge modes (helical) are protected by the winding number. In the metallic state regime, p_x -wave, d_{xy} -wave, and $d_{x^2-y^2}$ -wave pairings host point nodes, which lead to a flat band or a sine curve state, as shown in Fig. 3. Note that a dash (—) indicates no surface state and/or the Chern number is ill defined.

Pairing symmetry	$E_g > 2 \Delta_0 $			$E_g < 2 \Delta_0 $			Metallic state		
	GS	SS	$(\mathcal{N}, \mathcal{W})$	GS	SS	$(\mathcal{N}, \mathcal{W})$	GS	SS	$(\mathcal{N}, \mathcal{W})$
s wave	Full gap	Chiral	(2,0)	Full gap	Chiral	(1,1)	Full gap	Chiral	(1,1)
p_x wave ($\mathbf{d} \parallel \hat{x}$)	Full gap	Chiral	(2,0)	Full gap	Chiral	(2,0)	Point node	Flat band	(—, 1)
p_x wave ($\mathbf{d} \parallel \hat{y}$)	Full gap	Chiral	(2,0)	Full gap	Helical	(0,2)	Point node	Sine curve	(—, 1)
p_x wave ($\mathbf{d} \parallel \hat{z}$)	Full gap	Chiral	(2,0)	Line node	—	(—, 0)	Line node	—	(—, 0)
p_y wave ($\mathbf{d} \parallel \hat{x}$)	Full gap	Chiral	(2,0)	Full gap	—	(0,0)	Point node	—	(—, 0)
p_y wave ($\mathbf{d} \parallel \hat{y}$)	Full gap	Chiral	(2,0)	Full gap	Chiral	(2,0)	Point node	—	(—, 0)
p_y wave ($\mathbf{d} \parallel \hat{z}$)	Full gap	Chiral	(2,0)	Line node	—	(—, 0)	Line node	—	(—, 0)
Chiral $p \pm ip$ wave	Full gap	Chiral	(2,0)	Line node	—	(—, 0)	Line node	—	(—, 0)
d_{xy} wave	Full gap	Chiral	(2,0)	Full gap	Chiral	(2,0)	Point node	Sine curve	(—, 0)
$d_{x^2-y^2}$ wave	Full gap	Chiral	(2,0)	Full gap	Chiral	(2,0)	Point node	Sine curve	(—, 1)
Chiral $d + id$ wave	Full gap	Chiral	(2,0)	Full gap	Chiral	(2,0)	Full gap	Chiral	(—1, 1)
Chiral $d - id$ wave	Full gap	Chiral	(2,0)	Full gap	Chiral	(2,0)	Full gap	Chiral	(3, 1)

shown in Figs. 3 and 4. In what follow, we overview emergent topological phases for each regime.

1. $E_g > 2|\Delta_0|$

In this regime, the topology of the QAH is mainly contributed to the surface states. We observe two chiral Majorana

edge modes for all the hybrid systems when $m < 0$. Their stability is ensured by the Chern number $\mathcal{N} = 2$.

2. $E_g < 2|\Delta_0|$

Once the magnitude of the pair potential exceeds the insulating gap, we find topological phases unique to

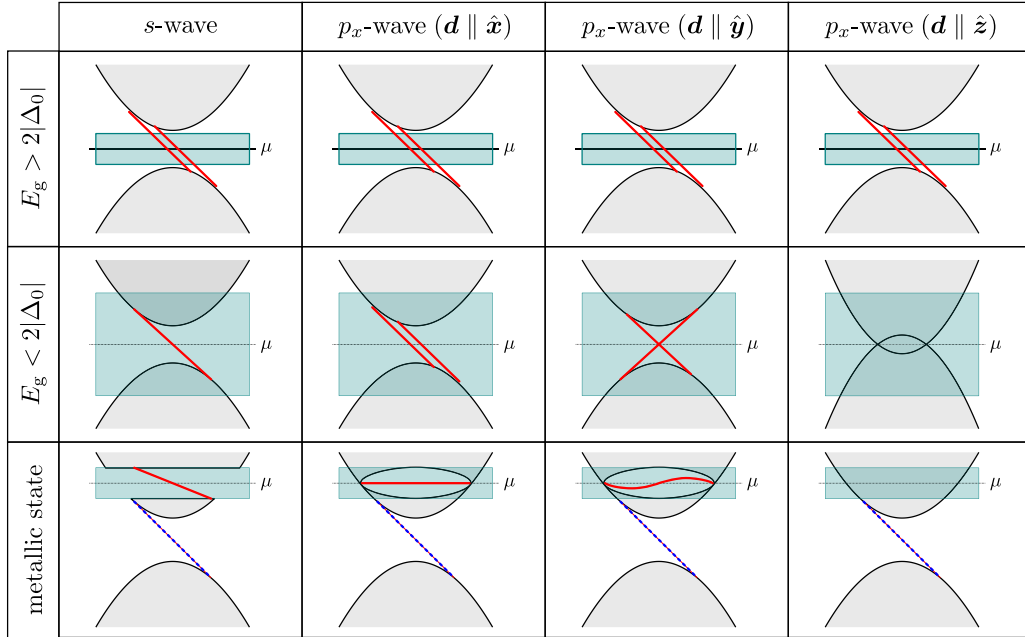


FIG. 3. Schematic illustration of SDOSs in the QAH/ s -wave and QAH/ p_x -wave SC hybrid systems. For the p_x -wave pairing, we choose the direction of the \mathbf{d} vector to be $\mathbf{d} \parallel \hat{x}$, $\mathbf{d} \parallel \hat{y}$, and $\mathbf{d} \parallel \hat{z}$. We illustrate surface states for three parameter regimes: $E_g > 2|\Delta_0|$, $E_g < 2|\Delta_0|$, and the metallic state, where E_g is the insulating gap and Δ_0 is the amplitude of the gap function. The red solid (blue dotted) lines represent edge states for superconducting QAHs (QAHs). The blue shaded areas describe the energy range of the gap function Δ_0 . We note that the direction of the Majorana edge modes is opposite to that predicted by the Chern numbers in Table II since the QAH/SC hybrid system is located at $x > 0$.

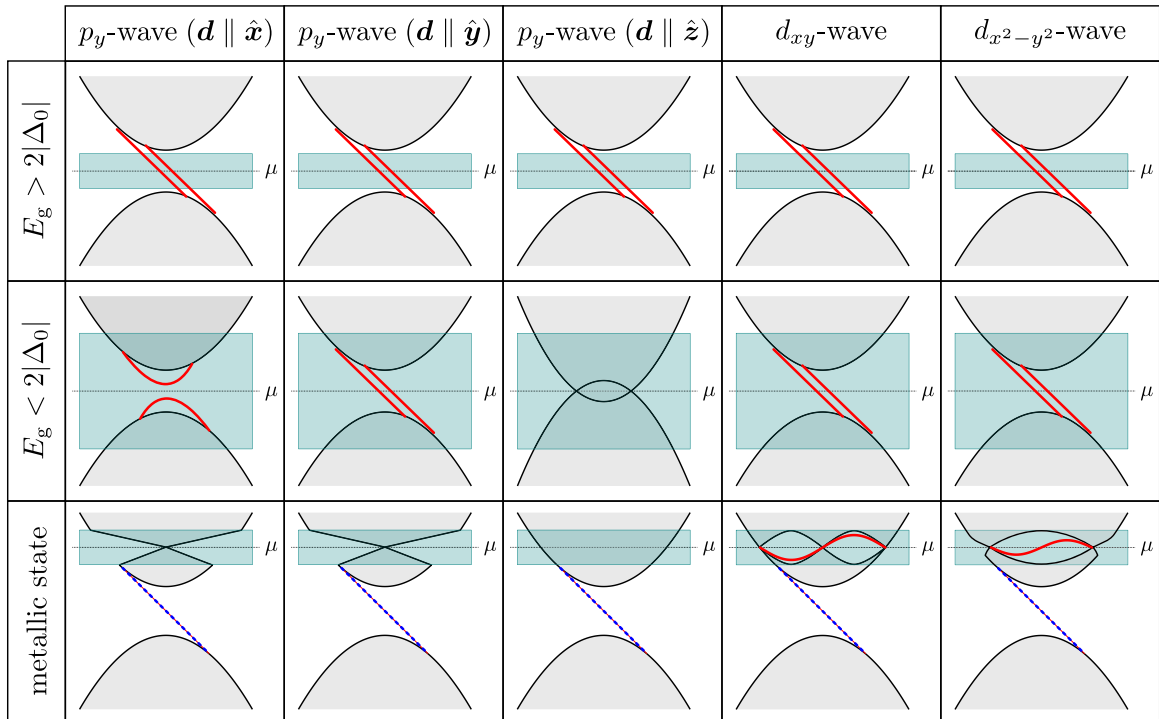


FIG. 4. Schematic illustration of SDOSs in the QAH/unconventional SC hybrid systems with p_y -wave, d_{xy} -wave, and $d_{x^2-y^2}$ -wave pairings.

unconventional pairings. For the p_x -wave ($\mathbf{d} \parallel \hat{x}$), p_y -wave ($\mathbf{d} \parallel \hat{y}$), and d -wave pairings, the two chiral Majorana edge modes appear again. On the other hand, a helical Majorana edge mode emerges for the p_x -wave pairing ($\mathbf{d} \parallel \hat{y}$). In this phase, the Chern number is zero, while the 1D crystalline-symmetry-protected winding number is nonzero. Thus, only the magnetic-reflection symmetry protects the helical Majorana edge mode. Note that the crystalline-symmetry-protected helical Majorana edge mode is distinguished from one protected by TRS since the system breaks TRS; see Sec. III B for more discussion.

Moreover, we find a line nodal phase, i.e., a completely gapless phase, for the p_x -wave ($\mathbf{d} \parallel \hat{z}$), p_y -wave ($\mathbf{d} \parallel \hat{z}$), and chiral p -wave pairings even when Δ_0 is finite. The line node originates from the mismatch of the spin structures between the QAH and the \mathbf{d} vector. We will show that the line node is protected by the 0D topological number in Sec. III C.

3. Metallic state

We tune the chemical potential to the metallic regime; that is, the Fermi level lies above or below the insulating gap. In this regime, the hybrid systems realize superconducting states inherent in unconventional pairings; the gap structures reflect the pairing symmetries except for the gapless phase. For gap functions with point nodes, surface states associated with point nodes emerge [109], where the spin-orbit coupling in the QAH gives a moderate change for some pairing symmetries. For instance, the p_x -wave pair ($\mathbf{d} \parallel \hat{y}$) has a surface sine curve state. The surface sine curve state is a dispersed surface state terminating at the point nodes (see Fig. 3) and is attributed to the spin-orbit coupling term in the QAH, which breaks the chiral symmetry (14) and can open a gap at $k_y \neq 0$ in the

surface. The same modifications also occur for the d_{xy} -wave and $d_{x^2-y^2}$ -wave pairings, whose surface densities of states exhibit a sine curve state [17,110] (see Fig. 4). Note that the sine curve states appear in the QAH/ $d_{x^2-y^2}$ -wave SC hybrid systems even when the $d_{x^2-y^2}$ -wave SC does not show any surface states on the (10) surface [111,112].

On the other hand, a fully gapped SC with multiple chiral Majorana edge modes is realized when the SC side has chiral $d \pm id$ -wave pairings, which host the nontrivial Chern number $\mathcal{N} = \mp 2$. The numerical calculation shows a sum rule of the Chern numbers: $1 - 2 = -1$ for the chiral $d + id$ -wave pairs and $1 + 2 = 3$ for the chiral $d - id$ -wave pairs, where the first (second) number represents the Chern number of the QAH (chiral SCs). Note that the sum rule also holds true for the s -wave case as $1 + 0 = 1$. To understand the sum rule of the QAH/chiral SC hybrid systems, we discuss an effective Hamiltonian projected onto the Fermi level in Sec. III D; the effective Hamiltonian explains the sum rule as the phase winding of an effective gap function.

B. Crystalline-symmetry-protected helical Majorana edge modes

It is known from the K -theoretical classification that 2D class-D SCs with magnetic-reflection symmetry are classified by double-integer numbers $\mathbb{Z} \times \mathbb{Z}$ [100], where the first and second numbers represent the Chern number \mathcal{N} and the 1D winding number \mathcal{W} defined in Sec. II C. Those topological numbers are not independent of each other, and a minimal set of topological numbers is given by $e_1 = (1, 1)$ and $e_2 = (1, -1) \in \mathbb{Z} \times \mathbb{Z}$ [100]. Other topological phases can be constructed from their combinations: $le_1 + me_2$ ($l, m \in \mathbb{Z}$). Thus, we find a topological phase without the Chern number

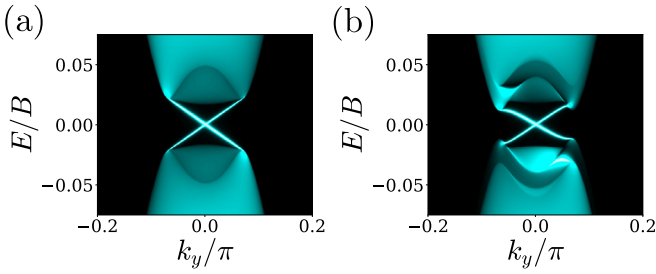


FIG. 5. SDOSs on the (10) surface for the QAH/ p_x -wave ($\mathbf{d} \parallel \hat{y}$) SC hybrid systems, where the parameters are chosen to be $(m, \Delta_0, \mu) = (-0.05, 0.175, 0)$ in (a) and $(-0.05, 0.175, 0.01)$ in (b).

when the topological number is proportional to $e_1 - e_2$. In this phase, the Chern numbers of e_1 and e_2 are canceled out, whereas the 1D winding number remains nonzero and takes an even integer. As a result, two chiral Majorana edge modes flow in the opposite direction, but a gap opening perturbation between them is prohibited by the 1D winding number protected by the magnetic-reflection symmetry; the resultant surface state turns out to be a crystalline-symmetry-protected helical Majorana edge mode even when TRS is absent.

From the calculation of topological numbers, we find the topological phase with $(\mathcal{N}, \mathcal{W}) = (0, 2)$ when the pairing symmetry on the SC side is the p_x -wave pairing ($\mathbf{d} \parallel \hat{y}$) (see Table II). As expected, the obtained SDOS shows the crystalline-symmetry-protected helical Majorana edge mode with a band crossing at $k_y = 0$ in Fig. 5(a). Furthermore, when $\mu \neq 0$, each counterpropagating edge mode has different velocities since the surface states do not need to respect TRS [see Fig. 5(b)]. This property makes a sharp contrast to the conventional helical Majorana edge mode protected by TRS.

We show a topological phase diagram of the QAH/ p_x -wave ($\mathbf{d} \parallel \hat{y}$) SC hybrid systems in Fig. 6, where the phase boundary is determined from the gap closing of the energy spectrum as it signals topological phase transitions. When

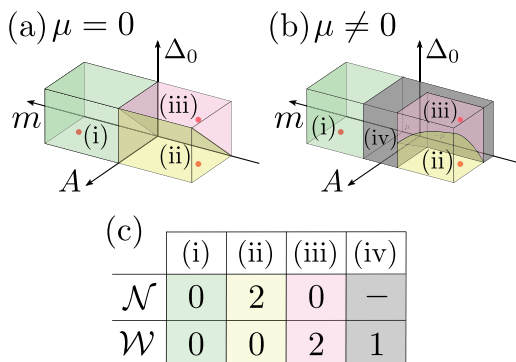


FIG. 6. Topological phase diagrams of the QAH/ p_x -wave ($\mathbf{d} \parallel \hat{y}$) SC hybrid systems for (a) $\mu = 0$ and (b) $\mu \neq 0$ as a function of the mass term m , the spin-orbit coupling A , and the gap function Δ_0 . (c) The topological numbers in each phase: (i) a fully gapped topologically trivial phase, (ii) a fully gapped topological phase with the two chiral Majorana edge modes, (iii) one with the crystalline-symmetry-protected helical Majorana edge modes, and (iv) a point node phase with a sine curve state.

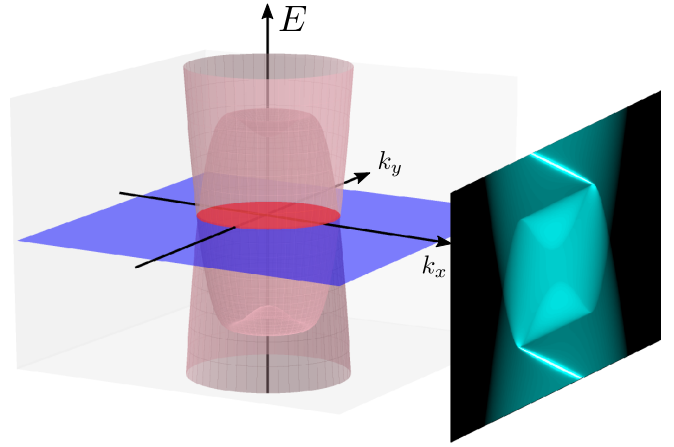


FIG. 7. The bulk energy spectrum (left) and the SDOS on the (10) surface (right) in the QAH/ p_y -wave ($\mathbf{d} \parallel \hat{z}$) SC hybrid system with the parameters $(m, \Delta_0, \mu) = (-0.05, 0.025, 0.06)$. The numerical calculation shows a line node (a gapless phase) due to the mismatch of the spin structure between the QAH state and \mathbf{d} vector.

$\mu = 0$, topological phases are divided into three regimes: (i) a fully gapped topologically trivial phase classified by $(\mathcal{N}, \mathcal{W}) = (0, 0)$ for $m > 0$, (ii) a fully gapped topological phase with the two chiral Majorana edge modes classified by $(2, 0)$ for $A > \Delta_0$ and $m < 0$, and (iii) one with the crystalline-symmetry-protected helical Majorana edge mode classified by $(0, 2)$ for $A < \Delta_0$ and $m < 0$ [see Fig. 6(a)]. (iv) On the other hand, when $\mu \neq 0$, a point node phase with $\mathcal{W} = 1$ appears in between the topologically trivial and nontrivial phases. In this phase, a surface sine curve state associated with the point nodes appears. The fully gapped topological phases remain stable in the parameter regime [see Fig. 6(b)].

C. Crystalline-symmetry-protected Bogoliubov Fermi surface

Our numerical calculations show a line node phase, i.e., a completely gapless phase, when the \mathbf{d} vector is parallel to the z axis (see Fig. 7). The gapless phase originates from the mismatch of spin structures between the QAH and the gap function. We here discuss the topological stability of the line node. The QAH/ p -wave ($\mathbf{d} \parallel \hat{z}$) SC hybrid system possesses neither TRS nor spatial-inversion symmetry. Instead, it has twofold rotation symmetry (7), which plays the same role as the spatial-inversion symmetry in 2D space. When the SC side has the \mathbf{d} vector parallel to the z axis, it yields the commutation relation $\{\mathcal{C}, \mathcal{C}_{2z}\} = 0$, which enables us to define a crystalline-symmetry-protected 0D \mathbb{Z}_2 invariant (21) that protects a line node even for odd-parity SCs. We note that the \mathbb{Z}_2 invariant is a generalization of that defined in three-dimensional even-parity SCs without TRS [101–106].

To verify that the line node is protected by the crystalline-symmetry-protected \mathbb{Z}_2 invariant, we numerically calculate Eq. (21) in the gapless phases in the QAH/ p_y -wave ($\mathbf{d} \parallel \hat{z}$) SC hybrid system. Figures 8(a) and 8(b) show the SDOSs for $E_g < 2|\Delta_0|$ and the metallic state, respectively. Both cases exhibit line nodes at the intersection of electron and hole bands. Figures 8(c) and 8(d) illustrate the sign of the Pfaffian in Eq. (21) for $E_g < 2|\Delta_0|$ and the metallic state, where we fix

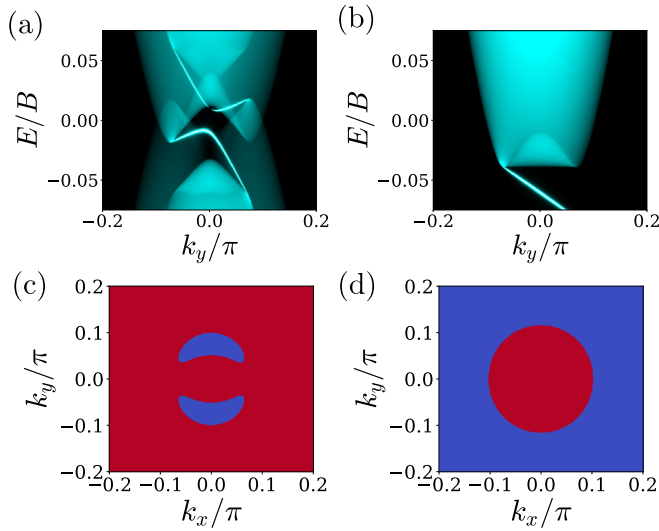


FIG. 8. SDOSs on the (10) surface and the sign of the Pfaffian in the QAH/ p_y -wave ($d \parallel \hat{z}$) SC hybrid system, where the parameters are chosen to be $(m, \Delta_0, \mu) = (-0.05, 0.175, 0)$ in (a) and (c) and $(-0.05, 0.025, 0.06)$ in (b) and (d); these parameters belong to the cases with $E_g < 2|\Delta_0|$ and the metallic state, respectively. In (a) and (b), the SDOSs exhibit a line node on the intersection of the electron and hole bands. In (c) and (d), we show the sign of the Pfaffian in Eq. (21) at $E = 0$, where \mathbf{k}'' is fixed to $(0,0)$. Red (blue) represents the region with $\nu = 0$ ($\nu = 1$). The sign change, which is the boundary between the red and blue regions, corresponds to the line node.

$\mathbf{k}'' = (0, 0)$ and vary \mathbf{k}' . The line nodes appear on the boundary of the regions with $\nu = 0$ (red) and $\nu = 1$ (blue); namely, they are protected by the crystalline-symmetry-protected \mathbb{Z}_2 invariant.

D. Multiple chiral Majorana edge modes

When the chemical potential lies above or below the insulating gap, the normal Hamiltonian forms a Fermi surface, and a superconducting gap arises on it. Then, superconducting states inherent in pairing symmetries arise in conjunction with a modification by the spin-orbit coupling in the QAH. In this regime, we find multiple chiral Majorana edge modes in the QAH/chiral ($d \pm id$)-wave SC hybrid systems since the chiral ($d \pm id$)-wave SCs have nonzero Chern numbers, which manifest chiral Majorana edge modes. However, the number of chiral Majorana edge modes in the hybrid system is different from that in the chiral ($d \pm id$)-wave SC. The reason is the Chern number in the QAH also affects the bulk topology, and thus, the number of chiral Majorana edge modes obeys a sum rule of the Chern numbers in the QAH and the chiral ($d \pm id$)-wave SC.

Figure 9 shows the SDOSs of QAH/chiral ($d \pm id$)-wave SC hybrid systems in the metallic regime. We find three chiral Majorana edge modes ($dE/dk_y < 0$) for the ($d - id$)-wave pairing and a single chiral Majorana edge mode ($dE/dk_y > 0$) for the ($d + id$)-wave pairing. Since the chiral ($d \pm id$)-wave SCs have Chern number $\mathcal{N} = \mp 2$, the Chern number in the hybrid systems is shifted by 1.

To understand the sum rule of the Chern numbers, we employ the analogy between superconducting Dirac Hamilto-

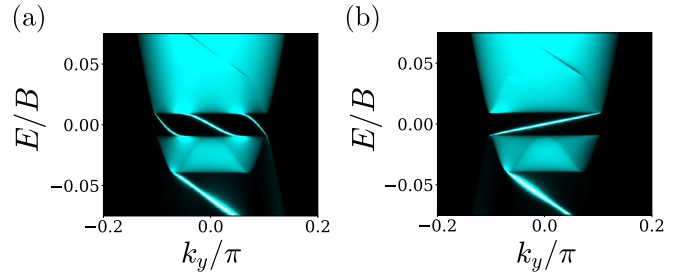


FIG. 9. SDOSs on the (10) surface in the QAH/ $(d \pm id)$ -wave SC hybrid systems with $(m, \Delta_0, \mu) = (-0.05, 0.175, 0.06)$. The SDOSs exhibit (a) three chiral Majorana edge modes for the ($d - id$)-wave pairing and (b) a single chiral Majorana edge mode for the ($d + id$)-wave pairing. Here, we enlarge Δ_0 to check the chiral Majorana edge modes. The superconducting gap on the Fermi surface is given by Eq. (27).

nians and spinless chiral p -wave superconductors [113,114]. The analogy is made by projecting the BdG Hamiltonian (2) onto the Fermi surface. Provided that $\mu \sim v|\mathbf{k}|$ and $\mu \gg E_g = 2|m|$, we can ignore $m(\mathbf{k})$, and the normal Hamiltonian is diagonalized by the unitary transformation,

$$\begin{pmatrix} \tilde{c}_{\mathbf{k},\uparrow} \\ \tilde{c}_{\mathbf{k},\downarrow} \end{pmatrix} \equiv \frac{1}{\sqrt{2}} \begin{pmatrix} 1 & e^{-i\theta_{\mathbf{k}}} \\ e^{i\theta_{\mathbf{k}}} & -1 \end{pmatrix} \begin{pmatrix} c_{\mathbf{k},\uparrow} \\ c_{\mathbf{k},\downarrow} \end{pmatrix}, \quad (24)$$

where $\theta_{\mathbf{k}} = \arctan(k_y/k_x)$. The projected Hamiltonian with the basis $\tilde{c}_{\mathbf{k},\uparrow}$ is then described as

$$\tilde{H}_{\text{BdG}} = (v|\mathbf{k}| - \mu)\tilde{c}_{\mathbf{k},\uparrow}^\dagger \tilde{c}_{\mathbf{k},\uparrow} + \frac{\Delta_0}{2} \{f(\mathbf{k})e^{-i\theta_{\mathbf{k}}} \tilde{c}_{\mathbf{k},\uparrow}^\dagger \tilde{c}_{\mathbf{k},\uparrow}^\dagger + \text{H.c.}\}. \quad (25)$$

Combined with Eq. (4), Eq. (25) has an effective gap function of

$$\tilde{\Delta}(\mathbf{k}) \equiv \begin{cases} \Delta_0 e^{-i\theta_{\mathbf{k}}} & (s \text{ wave}), \\ \Delta_0 |\mathbf{k}|^2 e^{i\theta_{\mathbf{k}}} & (\text{chiral } d + id \text{ wave}), \\ \Delta_0 |\mathbf{k}|^2 e^{-3i\theta_{\mathbf{k}}} & (\text{chiral } d - id \text{ wave}). \end{cases} \quad (26)$$

The results are consistent with the numerical calculation and show that the sum rule of the Chern number is interpreted as the change in the phase winding in the effective gap function. In a similar way, in the hole-doping regime ($\mu \ll -E_g$), we also have the sum rule of the Chern number by reversing the sign of the phase winding in the QAH. Note that the similar results hold true even when $m(\mathbf{k}) \neq 0$. In this case, the effective gap function is obtained as

$$\tilde{\Delta}(\mathbf{k}) = \frac{A|\mathbf{k}|}{E_{\text{QAH}}} \Delta_0 f(\mathbf{k}) e^{-i\theta_{\mathbf{k}}}. \quad (27)$$

IV. DISCUSSION AND CONCLUSION

In this paper, we have studied QAH/unconventional SC hybrid systems with p_x -wave, p_y -wave, d_{xy} -wave, $d_{x^2-y^2}$ -wave, chiral ($p \pm ip$)-wave, and chiral ($d \pm id$)-wave pairings. By focusing on the three characteristic parameter regimes and numerically calculating the SDOSs and the topological numbers, we have found a variety of topological phases with exotic topological phases enabled by the interplay between the QAH and unconventional SCs. The gap structure,

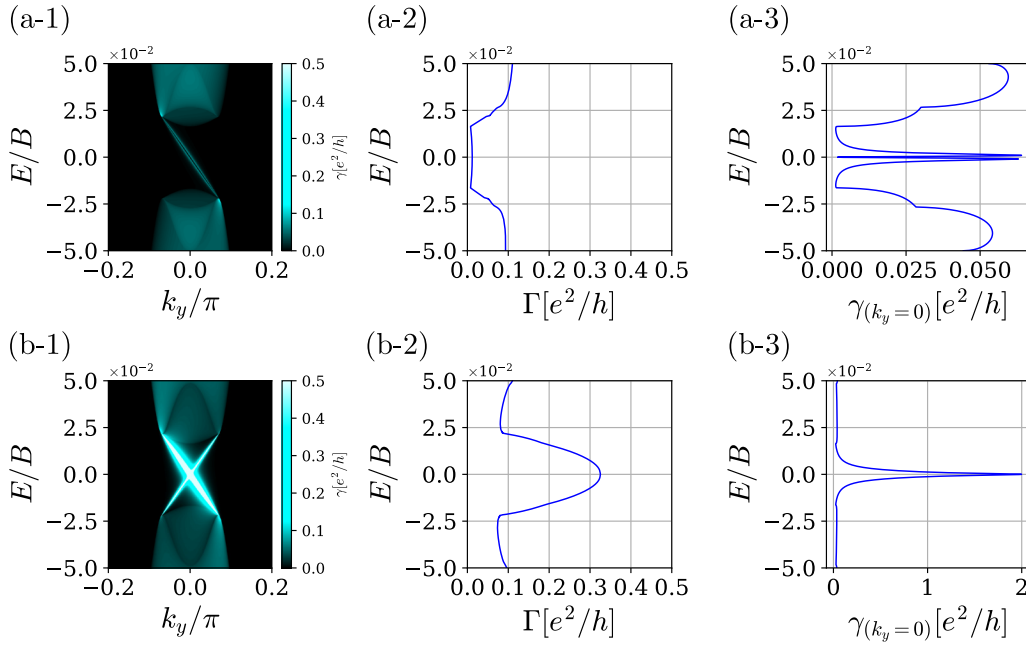


FIG. 10. Tunneling conductance in the normal metal/QAH/ p_x -wave ($\mathbf{d} \parallel \hat{y}$) SC junction. The angle-resolved conductance, the total conductance, and the angle-resolved conductance at $k_y = 0$ in the case of (a1)–(a3) $(\mathcal{N}, \mathcal{W}) = (2, 0)$ and (b1)–(b3) $(0, 2)$, respectively. Here, we define the normal metal as $H_N = 2t_N(2 - \cos k_x - \cos k_y) - \mu_N$, whose parameters are chosen to be $(t_N, \mu_N) = (10, 10)$. In the QAH/ p_x -wave ($\mathbf{d} \parallel \hat{y}$) SC hybrid system, we choose $(A, B, m, \Delta_0, \mu) = (0.1, 1, -0.05, 0.025, 0)$ for (a1), (a2), and (a3) and $(0.1, 1, -0.05, 0.175, 0)$ for (b1), (b2), and (b3).

surface states, and topological numbers are summarized in Table II, and the characteristic surface states are illustrated in Figs. 3 and 4. We have unveiled distinctive topological phases with crystalline-symmetry-protected helical Majorana edge modes (Sec. III B), crystalline-symmetry-protected Bogoliubov Fermi surfaces (line nodes; Sec. III C), and multiple chiral Majorana edge modes (Sec. III D). In particular, unlike the (pseudo-)TRS-protected helical Majorana edge modes [57,115], the crystalline-symmetry-protected helical Majorana edge modes do not respect TRS and allow counter-propagating edge currents with different velocities. The large variety of topological phases offers a platform for systematic study of topological phases and enables us to design exotic topological SCs experimentally.

Finally, we discuss tunnel conductance in a junction between a normal metal ($x > 0$) and the QAH/unconventional SC hybrid systems ($x < 0$) as a probe of the topological phases, which can be determined from the SDOSs and the topological numbers [43,109,112,116–123]. The behavior of tunnel conductance is briefly summarized as follows. Hereafter, we assume a normal metal without spin-orbit coupling with quadratic dispersion and an insulating barrier between the normal metal and the QAH/unconventional hybrid system in the metallic regime. The periodic boundary condition is imposed for the y axis, and the angle-resolved conductance is defined in terms of k_y .

(i) Tunnel conductance depends on the 1D winding number when the QAH/SC hybrid systems have a full gap and show topological surface states [43,116]; the angle-resolved conductance becomes enhanced in the gap and shows a zero-bias conductance peak at $k_y = 0$ when \mathcal{W} is nonzero, while the vanishing of conductance occurs when \mathcal{W} is zero due

to the interference of degenerate Majorana fermions [99]. This scenario can be applied to the topological phases with $(\mathcal{N}, \mathcal{W}) = (-1, 1), (1, 1), (2, 0), (0, 2),$ and $(3, 1)$, including the QAH/ p_x -wave ($\mathbf{d} \parallel \hat{y}$) SC hybrid systems showing the crystalline-symmetry-protected helical Majorana edge modes.

(ii) Tunnel conductance directly reflects the bulk density of states when the superconducting state has nodes but a surface state is absent [112]. In particular, the crystalline-symmetry-protected Bogoliubov Fermi surface behaves like a normal Fermi surface and thus can be observed as finite zero-bias conductance in the absence of the insulating barrier [123].

(iii) Tunnel conductance exhibits a sharp zero-bias conductance peak (a broadened zero-bias conductance peak) when the superconducting state has point nodes involving a surface flat band (a surface sine-curve state). Such behaviors have been studied in the context of unconventional SCs [109,112,117–122].

We numerically calculate tunnel conductance in a junction between a normal metal ($x > 0$) and the QAH/ p_x -wave ($\mathbf{d} \parallel \hat{y}$) SC hybrid system ($x < 0$) using the Lee-Fisher formula [43,124] to understand the difference between the chiral and helical Majorana edge modes classified by $(\mathcal{N}, \mathcal{W}) = (2, 0)$ and $(0, 2)$, where the angle-resolved conductance and the total conductance are defined by $\gamma(k_y, E)$ and $\Gamma(E) = \sum_{k_y} \gamma(k_y, E)$; see Ref. [43] for the explicit expressions.

Figure 10 shows the tunnel conductance in the normal metal/[QAH/ p_x -wave ($\mathbf{d} \parallel \hat{y}$) SC junction. We here consider the two parameter regimes, $E_g > 2|\Delta_0|$ and $E_g < 2|\Delta_0|$, for the purposes of comparison; their topological numbers are given by $(\mathcal{N}, \mathcal{W}) = (2, 0)$ and $(\mathcal{N}, \mathcal{W}) = (0, 2)$, respectively.

For $(\mathcal{N}, \mathcal{W}) = (2, 0)$, we find two chiral Majorana edge modes on the (10) surface [Fig. 10(a1)]. The total conductance decreases and is close to zero in the gap [see Fig. 10(a2)], whereas the angle-resolved conductance at $k_y = 0$ drastically vanishes at $E = 0$ [Fig. 10(a3)]. The vanishing of the conductance results from the degeneracy of the zero modes at $k_y = 0$ being accidental and not protected by any symmetry [43,99]. On the other hand, for $(\mathcal{N}, \mathcal{W}) = (0, 2)$, the crystalline-symmetry-protected helical Majorana edge modes appear on the (10) surface [Fig. 10(b1)] and significantly affect the conductance; the total conductance increases in the gap and peaks at $E = 0$ [Fig. 10(b2)], and the angle-resolved conductance at $k_y = 0$ exhibits a sharp zero-bias peak at $E = 0$ owing to the nonzero 1D winding number [Fig. 10(b3)]. The results are consistent with previous studies [43,116], and thus, the chiral

and helical Majorana edge modes are distinguishable though the tunnel conductance.

ACKNOWLEDGMENTS

R.O. was supported by JSPS KAKENHI Grant No. JP21J15526. S.K. was supported by JSPS KAKENHI Grants No. JP19K14612 and No. JP19H01824 and the CREST project (JPMJCR16F2, JPMJCR19T2) from the Japan Science and Technology Agency (JST). Y.T. was supported by Scientific Research (A) (KAKENHI Grant No. JP20H00131), Scientific Research (B) (KAKENHI Grants No. JP18H01176 and No. JP20H01857), Japan-RFBR Bilateral Joint Research Projects/Seminars No. 19-52-50026, and the JSPS Core-to-Core program “Oxide Superspin” international network.

-
- [1] X.-L. Qi and S.-C. Zhang, *Rev. Mod. Phys.* **83**, 1057 (2011).
 [2] Y. Tanaka, M. Sato, and N. Nagaosa, *J. Phys. Soc. Jpn.* **81**, 011013 (2012).
 [3] J. Alicea, *Rep. Prog. Phys.* **75**, 076501 (2012).
 [4] S. R. Elliott and M. Franz, *Rev. Mod. Phys.* **87**, 137 (2015).
 [5] M. Sato and S. Fujimoto, *J. Phys. Soc. Jpn.* **85**, 072001 (2016).
 [6] T. Mizushima, Y. Tsutsumi, T. Kawakami, M. Sato, M. Ichioka, and K. Machida, *J. Phys. Soc. Jpn.* **85**, 022001 (2016).
 [7] M. Sato and Y. Ando, *Rep. Prog. Phys.* **80**, 076501 (2017).
 [8] C.-K. Chiu, J. C. Y. Teo, A. P. Schnyder, and S. Ryu, *Rev. Mod. Phys.* **88**, 035005 (2016).
 [9] G. Moore and N. Read, *Nucl. Phys. B* **360**, 362 (1991).
 [10] N. Read and D. Green, *Phys. Rev. B* **61**, 10267 (2000).
 [11] D. A. Ivanov, *Phys. Rev. Lett.* **86**, 268 (2001).
 [12] M. Stone and S.-B. Chung, *Phys. Rev. B* **73**, 014505 (2006).
 [13] S. Fujimoto, *Phys. Rev. B* **77**, 220501(R) (2008).
 [14] J. Alicea, Y. Oreg, G. Refael, F. Von Oppen, and M. P. Fisher, *Nat. Phys.* **7**, 412 (2011).
 [15] C. Nayak, S. H. Simon, A. Stern, M. Freedman, and S. Das Sarma, *Rev. Mod. Phys.* **80**, 1083 (2008).
 [16] A. Y. Kitaev, *Phys. Usp.* **44**, 131 (2001).
 [17] M. Sato and S. Fujimoto, *Phys. Rev. B* **79**, 094504 (2009).
 [18] J. D. Sau, R. M. Lutchyn, S. Tewari, and S. Das Sarma, *Phys. Rev. Lett.* **104**, 040502 (2010).
 [19] J. Alicea, *Phys. Rev. B* **81**, 125318 (2010).
 [20] Y. Oreg, G. Refael, and F. von Oppen, *Phys. Rev. Lett.* **105**, 177002 (2010).
 [21] A. Cook and M. Franz, *Phys. Rev. B* **84**, 201105(R) (2011).
 [22] V. Mourik, K. Zuo, S. M. Frolov, S. R. Plissard, E. P. A. M. Bakkers, and L. P. Kouwenhoven, *Science* **336**, 1003 (2012).
 [23] A. Das, Y. Ronen, Y. Most, Y. Oreg, M. Heiblum, and H. Shtrikman, *Nat. Phys.* **8**, 887 (2012).
 [24] L. P. Rokhinson, X. Liu, and J. K. Furdyna, *Nat. Phys.* **8**, 795 (2012).
 [25] M. Deng, C. Yu, G. Huang, M. Larsson, P. Caroff, and H. Xu, *Nano Lett.* **12**, 6414 (2012).
 [26] A. D. K. Finck, D. J. Van Harlingen, P. K. Mohseni, K. Jung, and X. Li, *Phys. Rev. Lett.* **110**, 126406 (2013).
 [27] M. T. Deng, S. Vaitiekėnas, E. B. Hansen, J. Danon, M. Leijnse, K. Flensberg, J. Nygård, P. Krogstrup, and C. M. Marcus, *Science* **354**, 1557 (2016).
 [28] T.-P. Choy, J. M. Edge, A. R. Akhmerov, and C. W. J. Beenakker, *Phys. Rev. B* **84**, 195442 (2011).
 [29] B. Braunecker and P. Simon, *Phys. Rev. Lett.* **111**, 147202 (2013).
 [30] J. Klinovaja, P. Stano, A. Yazdani, and D. Loss, *Phys. Rev. Lett.* **111**, 186805 (2013).
 [31] S. Nadj-Perge, I. K. Drozdov, B. A. Bernevig, and A. Yazdani, *Phys. Rev. B* **88**, 020407(R) (2013).
 [32] M. M. Vazifeh and M. Franz, *Phys. Rev. Lett.* **111**, 206802 (2013).
 [33] S. Nadj-Perge, I. K. Drozdov, J. Li, H. Chen, S. Jeon, J. Seo, A. H. MacDonald, B. A. Bernevig, and A. Yazdani, *Science* **346**, 602 (2014).
 [34] M. Ruby, F. Pientka, Y. Peng, F. von Oppen, B. W. Heinrich, and K. J. Franke, *Phys. Rev. Lett.* **115**, 197204 (2015).
 [35] R. Pawlak, M. Kisiel, J. Klinovaja, T. Meier, S. Kawai, T. Glatzel, D. Loss, and E. Meyer, *npj Quantum Inf.* **2**, 16035 (2016).
 [36] S. Jeon, Y. Xie, J. Li, Z. Wang, B. A. Bernevig, and A. Yazdani, *Science* **358**, 772 (2017).
 [37] H. Kim, A. Palacio-Morales, T. Posske, L. Rózsa, K. Palotás, L. Szunyogh, M. Thorwart, and R. Wiesendanger, *Sci. Adv.* **4**, eaar5251 (2018).
 [38] F. D. M. Haldane, *Phys. Rev. Lett.* **61**, 2015 (1988).
 [39] R. Yu, W. Zhang, H.-J. Zhang, S.-C. Zhang, X. Dai, and Z. Fang, *Science* **329**, 61 (2010).
 [40] C.-Z. Chang *et al.*, *Science* **340**, 167 (2013).
 [41] X.-L. Qi, T. L. Hughes, and S.-C. Zhang, *Phys. Rev. B* **82**, 184516 (2010).
 [42] A. Ii, K. Yada, M. Sato, and Y. Tanaka, *Phys. Rev. B* **83**, 224524 (2011).
 [43] A. Ii, A. Yamakage, K. Yada, M. Sato, and Y. Tanaka, *Phys. Rev. B* **86**, 174512 (2012).
 [44] J. J. He, J. Wu, T.-P. Choy, X.-J. Liu, Y. Tanaka, and K. T. Law, *Nat. Commun.* **5**, 3232 (2014).
 [45] A. Altland and M. R. Zirnbauer, *Phys. Rev. B* **55**, 1142 (1997).
 [46] M. R. Zirnbauer, *J. Math. Phys.* **37**, 4986 (1996).
 [47] A. P. Schnyder, S. Ryu, A. Furusaki, and A. W. W. Ludwig, *Phys. Rev. B* **78**, 195125 (2008).

- [48] A. Kitaev, in *Advances in Theoretical Physics: Landau Memorial Conference*, AIP Conf. Proc. No. 1134 (AIP, Melville, NY, 2009), p. 22.
- [49] A. P. Schnyder, S. Ryu, A. Furusaki, and A. W. W. Ludwig, in *Advances in Theoretical Physics: Landau Memorial Conference*, AIP Conf. Proc. No. 1134 (AIP, Melville, NY, 2009), p. 10.
- [50] S. Ryu, A. P. Schnyder, A. Furusaki, and A. W. W. Ludwig, *New J. Phys.* **12**, 065010 (2010).
- [51] Q. L. He, L. Pan, A. L. Stern, E. C. Burks, X. Che, G. Yin, J. Wang, B. Lian, Q. Zhou, E. S. Choi, K. Murata, X. Kou, Z. Chen, T. Nie, Q. Shao, Y. Fan, S.-C. Zhang, K. Liu, J. Xia, and K. L. Wang, *Science* **357**, 294 (2017).
- [52] S. B. Chung, X.-L. Qi, J. Maciejko, and S.-C. Zhang, *Phys. Rev. B* **83**, 100512(R) (2011).
- [53] J. Wang, Q. Zhou, B. Lian, and S.-C. Zhang, *Phys. Rev. B* **92**, 064520 (2015).
- [54] B. Lian, X.-Q. Sun, A. Vaezi, X.-L. Qi, and S.-C. Zhang, *Proc. Natl. Acad. Sci. USA* **115**, 10938 (2018).
- [55] K. Yasuda, M. Mogi, R. Yoshimi, A. Tsukazaki, K. S. Takahashi, M. Kawasaki, F. Kagawa, and Y. Tokura, *Science* **358**, 1311 (2017).
- [56] W. Ji and X.-G. Wen, *Phys. Rev. Lett.* **120**, 107002 (2018).
- [57] Y. Huang, F. Setiawan, and J. D. Sau, *Phys. Rev. B* **97**, 100501(R) (2018).
- [58] M. Kayyalha, D. Xiao, R. Zhang, J. Shin, J. Jiang, F. Wang, Y.-F. Zhao, R. Xiao, L. Zhang, K. M. Fijalkowski, P. Mandal, M. Winnerlein, C. Gould, Q. Li, L. W. Molenkamp, M. H. W. Chan, N. Samarth, and C.-Z. Chang, *Science* **367**, 64 (2020).
- [59] J. Shen, J. Lyu, J. Z. Gao, Y.-M. Xie, C.-Z. Chen, C.-W. Cho, O. Atanov, Z. Chen, K. Liu, Y. J. Hu, K. Y. Yip, S. K. Goh, Q. L. He, L. Pan, K. L. Wang, K. T. Law, and R. Lortz, *Proc. Natl. Acad. Sci. USA* **117**, 238 (2020).
- [60] J. L. Lado and M. Sigrist, *Phys. Rev. Lett.* **121**, 037002 (2018).
- [61] J. Wang and B. Lian, *Phys. Rev. Lett.* **121**, 256801 (2018).
- [62] J. J. He, T. Liang, Y. Tanaka, and N. Nagaosa, *Commun. Phys.* **2**, 149 (2019).
- [63] L. Fu and E. Berg, *Phys. Rev. Lett.* **105**, 097001 (2010).
- [64] M. Sato, *Phys. Rev. B* **81**, 220504(R) (2010).
- [65] A. Yamakage, K. Yada, M. Sato, and Y. Tanaka, *Phys. Rev. B* **85**, 180509(R) (2012).
- [66] T. Hashimoto, K. Yada, M. Sato, and Y. Tanaka, *Phys. Rev. B* **92**, 174527 (2015).
- [67] B. Lu, K. Yada, M. Sato, and Y. Tanaka, *Phys. Rev. Lett.* **114**, 096804 (2015).
- [68] S. Kobayashi and M. Sato, *Phys. Rev. Lett.* **115**, 187001 (2015).
- [69] T. Hashimoto, S. Kobayashi, Y. Tanaka, and M. Sato, *Phys. Rev. B* **94**, 014510 (2016).
- [70] M. Oudah, A. Ikeda, J. N. Hausmann, S. Yonezawa, T. Fukumoto, S. Kobayashi, M. Sato, and Y. Maeno, *Nat. Commun.* **7**, 13617 (2016).
- [71] T. Kawakami, T. Okamura, S. Kobayashi, and M. Sato, *Phys. Rev. X* **8**, 041026 (2018).
- [72] T. Kawakami and M. Sato, *Phys. Rev. B* **100**, 094520 (2019).
- [73] J. G. Bednorz and K. A. Müller, *Z. Phys. B* **64**, 189 (1986).
- [74] D. Scalapino, *Phys. Rep.* **250**, 329 (1995).
- [75] C. C. Tsuei and J. R. Kirtley, *Rev. Mod. Phys.* **72**, 969 (2000).
- [76] Y. Maeno, H. Hashimoto, K. Yoshida, S. Nishizaki, T. Fujita, J. Bednorz, and F. Lichtenberg, *Nature (London)* **372**, 532 (1994).
- [77] T. M. Rice and M. Sigrist, *J. Phys.: Condens. Matter* **7**, L643 (1995).
- [78] A. P. Mackenzie and Y. Maeno, *Rev. Mod. Phys.* **75**, 657 (2003).
- [79] Y. Maeno, S. Kittaka, T. Nomura, S. Yonezawa, and K. Ishida, *J. Phys. Soc. Jpn.* **81**, 011009 (2012).
- [80] A. Pustogow, Y. Luo, A. Chronister, Y.-S. Su, D. Sokolov, F. Jerzembeck, A. P. Mackenzie, C. W. Hicks, N. Kikugawa, S. Raghu, E. D. Bauer, and S. E. Brown, *Nature (London)* **574**, 72 (2019).
- [81] H. G. Suh, H. Menke, P. M. R. Brydon, C. Timm, A. Ramires, and D. F. Agterberg, *Phys. Rev. Res.* **2**, 032023(R) (2020).
- [82] O. Gingras, R. Nourafkan, A. M. S. Tremblay, and M. Côté, *Phys. Rev. Lett.* **123**, 217005 (2019).
- [83] H. S. Røising, T. Scaffidi, F. Flicker, G. F. Lange, and S. H. Simon, *Phys. Rev. Res.* **1**, 033108 (2019).
- [84] S. Ghosh, A. Shekhter, F. Jerzembeck, N. Kikugawa, D. A. Sokolov, M. Brando, A. Mackenzie, C. W. Hicks, and B. Ramshaw, *Nat. Phys.* **17**, 199 (2021).
- [85] V. Grinenko, S. Ghosh, R. Sarkar, J.-C. Orain, A. Nikitin, M. Elender, D. Das, Z. Guguchia, F. Brückner, M. E. Barber, J. Park, N. Kikugawa, D. A. Sokolov, J. S. Bobowski, T. Miyoshi, Y. Maeno, A. P. Mackenzie, H. Luetkens, C. W. Hicks, and H.-H. Klauss, *Nat. Phys.* **17**, 748 (2021).
- [86] S. Benhabib, C. Lupien, I. Paul, L. Berges, M. Dion, M. Nardone, A. Zitouni, Z. Mao, Y. Maeno, A. Georges, L. Taillefer, and C. Proust, *Nat. Phys.* **17**, 194 (2021).
- [87] Y. Nishikubo, K. Kudo, and M. Nohara, *J. Phys. Soc. Jpn.* **80**, 055002 (2011).
- [88] P. K. Biswas, H. Luetkens, T. Neupert, T. Stürzer, C. Baines, G. Pascua, A. P. Schnyder, M. H. Fischer, J. Goryo, M. R. Lees, H. Maeter, F. Brückner, H.-H. Klauss, M. Nicklas, P. J. Baker, A. D. Hillier, M. Sigrist, A. Amato, and D. Johrendt, *Phys. Rev. B* **87**, 180503(R) (2013).
- [89] M. H. Fischer, T. Neupert, C. Platt, A. P. Schnyder, W. Hanke, J. Goryo, R. Thomale, and M. Sigrist, *Phys. Rev. B* **89**, 020509(R) (2014).
- [90] J. A. Sauls, *Adv. Phys.* **43**, 113 (1994).
- [91] R. Joynt and L. Taillefer, *Rev. Mod. Phys.* **74**, 235 (2002).
- [92] J. D. Strand, D. J. Bahr, D. J. Van Harlingen, J. P. Davis, W. J. Gannon, and W. P. Halperin, *Science* **328**, 1368 (2010).
- [93] E. R. Schemm, W. J. Gannon, C. M. Wishne, W. P. Halperin, and A. Kapitulnik, *Science* **345**, 190 (2014).
- [94] Y. Kasahara, T. Iwasawa, H. Shishido, T. Shibauchi, K. Behnia, Y. Haga, T. D. Matsuda, Y. Onuki, M. Sigrist, and Y. Matsuda, *Phys. Rev. Lett.* **99**, 116402 (2007).
- [95] T. Shibauchi, H. Ikeda, and Y. Matsuda, *Philos. Mag.* **94**, 3747 (2014).
- [96] E. R. Schemm, R. E. Baumbach, P. H. Tobash, F. Ronning, E. D. Bauer, and A. Kapitulnik, *Phys. Rev. B* **91**, 140506(R) (2015).
- [97] S. Ran, C. Eckberg, Q.-P. Ding, Y. Furukawa, T. Metz, S. R. Saha, I.-L. Liu, M. Zic, H. Kim, J. Paglione, and N. P. Butch, *Science* **365**, 684 (2019).

- [98] L. Jiao, S. Howard, S. Ran, Z. Wang, J. O. Rodriguez, M. Sigrist, Z. Wang, N. P. Butch, and V. Madhavan, *Nature (London)* **579**, 523 (2020).
- [99] A. Yamakage and M. Sato, *Phys. E* **55**, 13 (2014).
- [100] K. Shiozaki and M. Sato, *Phys. Rev. B* **90**, 165114 (2014).
- [101] S. Kobayashi, K. Shiozaki, Y. Tanaka, and M. Sato, *Phys. Rev. B* **90**, 024516 (2014).
- [102] Y. X. Zhao, A. P. Schnyder, and Z. D. Wang, *Phys. Rev. Lett.* **116**, 156402 (2016).
- [103] D. F. Agterberg, P. M. R. Brydon, and C. Timm, *Phys. Rev. Lett.* **118**, 127001 (2017).
- [104] T. Bzdušek and M. Sigrist, *Phys. Rev. B* **96**, 155105 (2017).
- [105] C. Timm, A. P. Schnyder, D. F. Agterberg, and P. M. R. Brydon, *Phys. Rev. B* **96**, 094526 (2017).
- [106] P. M. R. Brydon, D. F. Agterberg, H. Menke, and C. Timm, *Phys. Rev. B* **98**, 224509 (2018).
- [107] A. Umerski, *Phys. Rev. B* **55**, 5266 (1997).
- [108] T. Fukui, Y. Hatsugai, and H. Suzuki, *J. Phys. Soc. Jpn.* **74**, 1674 (2005).
- [109] M. Sato, Y. Tanaka, K. Yada, and T. Yokoyama, *Phys. Rev. B* **83**, 224511 (2011).
- [110] M. Sato and S. Fujimoto, *Phys. Rev. Lett.* **105**, 217001 (2010).
- [111] C.-R. Hu, *Phys. Rev. Lett.* **72**, 1526 (1994).
- [112] S. Kashiwaya and Y. Tanaka, *Rep. Prog. Phys.* **63**, 1641 (2000).
- [113] L. Fu and C. L. Kane, *Phys. Rev. Lett.* **100**, 096407 (2008).
- [114] Y. Tanaka, T. Yokoyama, and N. Nagaosa, *Phys. Rev. Lett.* **103**, 107002 (2009).
- [115] X.-L. Qi, T. L. Hughes, S. Raghu, and S.-C. Zhang, *Phys. Rev. Lett.* **102**, 187001 (2009).
- [116] R. Ohashi, Y. Tanaka, and K. Yada, *J. Phys. Soc. Jpn.* **89**, 054701 (2020).
- [117] M. Matsumoto and H. Shiba, *J. Phys. Soc. Jpn.* **64**, 1703 (1995).
- [118] Y. Tanaka and S. Kashiwaya, *Phys. Rev. Lett.* **74**, 3451 (1995).
- [119] Y. Tanuma, Y. Tanaka, and S. Kashiwaya, *Phys. Rev. B* **64**, 214519 (2001).
- [120] K. Yada, M. Sato, Y. Tanaka, and T. Yokoyama, *Phys. Rev. B* **83**, 064505 (2011).
- [121] S. Kobayashi, Y. Tanaka, and M. Sato, *Phys. Rev. B* **92**, 214514 (2015).
- [122] S. Tamura, S. Kobayashi, L. Bo, and Y. Tanaka, *Phys. Rev. B* **95**, 104511 (2017).
- [123] C. J. Lapp, G. Börner, and C. Timm, *Phys. Rev. B* **101**, 024505 (2020).
- [124] P. A. Lee and D. S. Fisher, *Phys. Rev. Lett.* **47**, 882 (1981).